



Filaments from *Ignicoccus hospitalis* Show Diversity of Packing in Proteins Containing N-Terminal Type IV Pilin Helices

Xiong Yu¹, Charles Goforth¹, Carolin Meyer², Reinhard Rachel², Reinhard Wirth², Gunnar F. Schröder³ and Edward H. Egelman^{1*}

¹Department of Biochemistry and Molecular Genetics, University of Virginia, Box 800733, Charlottesville, VA 22908-0733, USA

²Department of Microbiology, Archaea Center, University of Regensburg, D-93053 Regensburg, Germany

³Institute of Complex Systems (ICS-6), Forschungszentrum Jülich, 52425 Jülich, Germany

Received 26 March 2012;
received in revised form

4 May 2012;
accepted 21 May 2012

Available online
30 May 2012

Edited by J. Johnson

Keywords:

electron microscopy;
helical polymers;
convergent evolution;
archaea

Bacterial motility is driven by the rotation of flagellar filaments that supercoil. The supercoiling involves the switching of coiled-coil protofilaments between two different states. In archaea, the flagellar filaments responsible for motility are formed by proteins with distinct homology in their N-terminal portion to bacterial Type IV pilins. The bacterial pilins have a single N-terminal hydrophobic α -helix, not the coiled coil found in flagellin. We have used electron cryo-microscopy to study the adhesion filaments from the archaeon *Ignicoccus hospitalis*. While *I. hospitalis* is non-motile, these filaments make transitions between rigid stretches and curved regions and appear morphologically similar to true archaeal flagellar filaments. A resolution of ~ 7.5 Å allows us to unambiguously build a model for the packing of these N-terminal α -helices, and this packing is different from several bacterial Type IV pili whose structure has been analyzed by electron microscopy and modeling. Our results show that the mechanism responsible for the supercoiling of bacterial flagellar filaments cannot apply to archaeal filaments.

© 2012 Elsevier Ltd. All rights reserved.

Introduction

Bacterial motility has been a fascinating topic for many reasons. One question has been how a homopolymer, assembled from the protein flagellin, can form helical filaments that supercoil.¹ For an

ideal helical polymer, every subunit must be in an equivalent environment, and this generates a straight filament. However, straight filaments generate no thrust when rotating, and mutant flagellins^{2,3} have been found to form such ideal straight filaments with a resulting non-motile phenotype. For a supercoiled filament, subunits on the inside of the supercoil are in a different environment than subunits on the outside, but this creates a problem since all subunits are chemically identical. The resolution of this problem^{1,4–9} involved a model for the flagella filament being composed of protofilaments that could discretely switch between two different states, one slightly longer in length than the other. The longer protofilaments would be found on the outside of the supercoil, while the shorter protofilaments would be

*Corresponding author. E-mail address: egelman@virginia.edu.

Present address: C. Meyer, Institute of Groundwater Ecology, German Research Center for Environmental Health, Ingolstädter Landstr. 1, 85764 Neuherberg, Germany.

Abbreviations used: cryo-EM, electron cryo-microscopy; TEM, transmission electron microscopy; EM, electron microscopy; FSC, Fourier shell correlation.

found on the inside,¹⁰ and the number of protofilaments in each state would determine the supercoil waveform. Detailed experimental studies by both X-ray fiber diffraction and electron cryo-microscopy (cryo-EM) have provided beautiful confirmation of this idea^{11–14} with models for both states of the protofilament at near-atomic resolution.

The protofilaments, 11 in the case of *Salmonella* and a number of other bacteria, but only 7 for *Campylobacter*,¹⁵ are formed by intrasubunit coiled coils involving the N- and C-terminal portions of flagellin.^{12,16,17} However, it has now become clear that archaeal flagellar filaments are formed not by homologs of bacterial flagellin but rather by proteins with distinct homology in their N-terminal portion to bacterial Type IV pilins.^{18–25} All Type IV pilins are characterized by a conserved single N-terminal α -helix formed almost entirely from hydrophobic residues.^{26–28} These pilins all have a signal sequence at the N-terminus that becomes cleaved and is not present in the mature pilin and have globular domains that are highly divergent, even among related species.^{29,30} The argument for homology between the archaeal flagellins and the bacterial Type IV pilins is supported by the similarity of the unusual signal sequences that are present in the preproteins and the homology of the signal peptidases in bacteria and archaea that cleave this signal sequence.^{22,31,32} Bacterial Type IV pilins assemble into pili that are involved in many activities, including adhesion and motility.³⁰

Since archaeal flagellar filaments supercoil, as do the bacterial ones, a fascinating question is whether the mechanism of supercoiling is similar between the two. Existing structural studies of archaeal flagellar filaments^{23–25} lack the resolution needed to see whether coiled coils might exist in these polymers and whether there are constituent protofilaments. We have used cryo-EM to study the Iho670 adhesion filaments³³ from the archaeon *Ignicoccus hospitalis*. This organism is non-motile; hence, these flagellar-like filaments that extend from the cell appear to be mainly involved in adhesion. Like bacterial Type IV pilins, Iho670 contains a short

signal peptide at the N-terminus that is cleaved and not found in the mature protein. Inspection of the processed Iho670 N-terminal sequence (Fig. 1) shows that residues 4–25 are all hydrophobic. A comparison of the N-terminal amino acids with several bacterial Type IV pilins and an archaeal flagellar filament protein (Fig. 1) shows the strong conservation of these hydrophobic residues. Consistent with the globular D2/D3 domains in bacterial flagellin³⁵ and the globular domains in bacterial Type IV pili³⁶ that are all hyper-variable, the remainder of the Iho670 sequence shows no sequence conservation with other proteins.

Results

The Iho670 filaments were initially examined by transmission electron microscopy (TEM) of negatively stained specimens both while attached to cells (Fig. 2a) and after being sheared off the cells (Fig. 2b). Intact cells (Fig. 2a) of *I. hospitalis* were grown directly on carbon-coated gold grids, and the fibers were previously identified as being composed of Iho670.^{33,37} Due to the high number of fibers present, it was often impossible to say which fiber belonged to which cell. Many filaments appeared to be quite rigid over distances of $\sim 20 \mu\text{m}$. On the other hand, regions were seen (Fig. 2a, black arrows) where the filaments had a sinusoidal curvature. The sinusoidal paths were not all identical in amplitude and period. These characteristic curves were frequently found when two fibers crossed each other but could also be found in isolated fibers. In addition, regions where the fibers looped about themselves were found (Fig. 2a, white arrows), completely inconsistent with the rigid appearance of these fibers in other areas. Similar images were obtained looking at many grids. These fibers were never exposed to any isolation procedure and were actually grown on the electron microscopy (EM) grids to reduce the chance of preparative artifacts; thus, we think that these observations represent the native characteristics of these filaments.

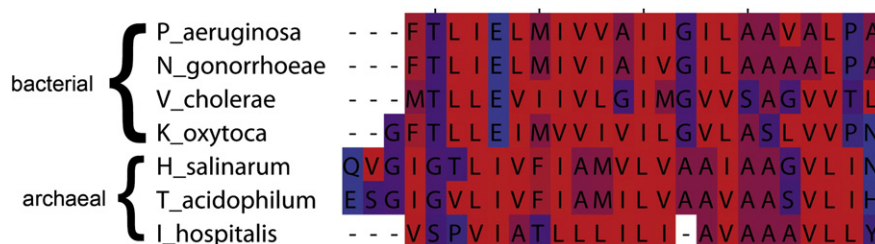


Fig. 1. A ClustalW alignment³⁴ of the N-termini of four bacterial Type IV pilins (*Pseudomonas aeruginosa* PilA from strain PAK; *Neisseria gonorrhoeae* PilE; *Klebsiella oxytoca* PulG; *Vibrio cholera* TcpA) with two archaeal flagellar proteins (*Halobacterium salinarum* FlgB2; *Thermoplasma acidophilum* FlaB) and the Iho670 protein from *Ignicoccus hospitalis*. The color code represents hydrophobicity, with red being the most hydrophobic and blue being hydrophilic.

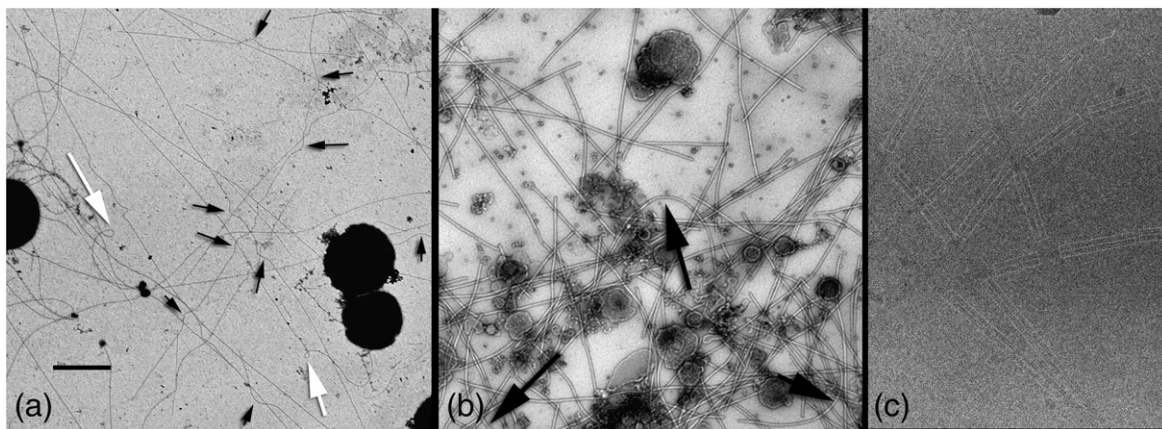


Fig. 2. Images of negatively stained (a and b) and unstained frozen/hydrated (c) Iho670 filaments. In (a), cells were grown on carbon-coated EM grids to avoid any mechanical damage to the filaments due to shear, transfer to the grids, and so forth. The black arrows point to regions where the filaments adopt a characteristic curved shape, which is frequently seen when one filament crosses over another one. The white arrows point to regions of what appear to be anomalous flexibility, where these normally rigid filaments can form tight loops. In (b), the filaments were sheared off the cells and concentrated. The black arrows (b) point to regions where the filaments undergo a bend of $\sim 180^\circ$. In (c), the boxes that have been placed around the filaments are 250 Å (200 px) in width. The scale bar in (a) represents 2 μm .

When the filaments were sheared off the cells and examined by negative-stain EM (Fig. 2b), they also appeared to behave anomalously. That is, they were inconsistent with the appearance of filaments having a uniform flexural rigidity whose curvature is driven by thermal forces.³⁸ Most of the filaments appeared quite rigid over long distances, but some (Fig. 2b, arrows) showed a characteristic curvature responsible for reversing the direction of the filament.

Electron cryo-microscopy

We used cryo-EM of unstained frozen/hydrated Iho670 for further image analysis (Fig. 2c). A total of 17 micrographs were used after eliminating those with any astigmatism, drift, or aggregation of the filaments. The defocus range was from 1.7 to 3.4 μm . A power spectrum (Fig. 3) calculated from the cryo-EM segments shows more than seven layer lines. Given that the one at $\sim 1/(17.9 \text{ Å})$ could only be either $n=+1$ or $n=-1$, the indexing of this pattern was relatively unambiguous, particularly since the two strongest layer lines (labeled $n=7$, $n=-3$ in Fig. 3) were of odd Bessel order based upon phase relations in Fourier transforms of EM images of negatively stained filaments. This contrasts with other helical specimens where substantial ambiguities may exist in the indexing of such patterns.^{39,40} The only ambiguity from this pattern is whether the layer line at $1/(17.9 \text{ Å})$ is $n=+1$ or $n=-1$. We show (below) that it is most likely to be $n=+1$; hence, we use that convention in the figure. The indexing scheme shown (Fig. 3) corresponds to ~ 3.4 subunits per turn of a 17.9-Å pitch helix.

These estimates for the helical symmetry were used in the IHRSR (iterative helical real-space reconstruction) procedure,⁴¹ starting with a solid cylinder as the initial reference. A total of 22,966

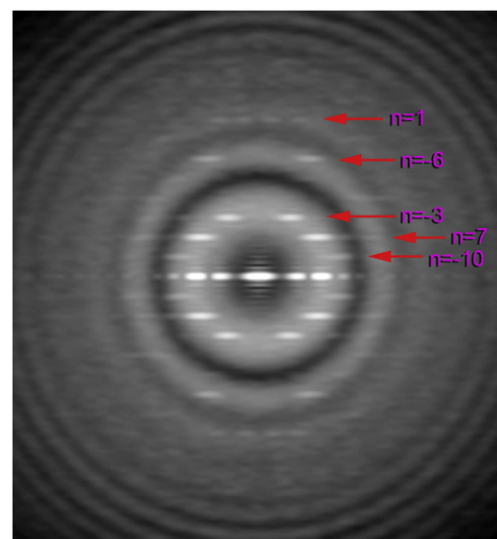


Fig. 3. A power spectrum computed from 14,731 overlapping segments of the Iho670 filaments (each segment is 500 Å long). The log of the power spectrum is shown to allow for the very large dynamic range. Because each image was first multiplied by the measured contrast transfer function to boost the overall signal-to-noise ratio in the images, the modulation of the pattern due to the contrast transfer function is readily apparent. The strongest layer lines are labeled with their Bessel orders, assuming that the layer line at $1/(17.9 \text{ Å})$ is $n=+1$, and not $n=-1$ (see the text).

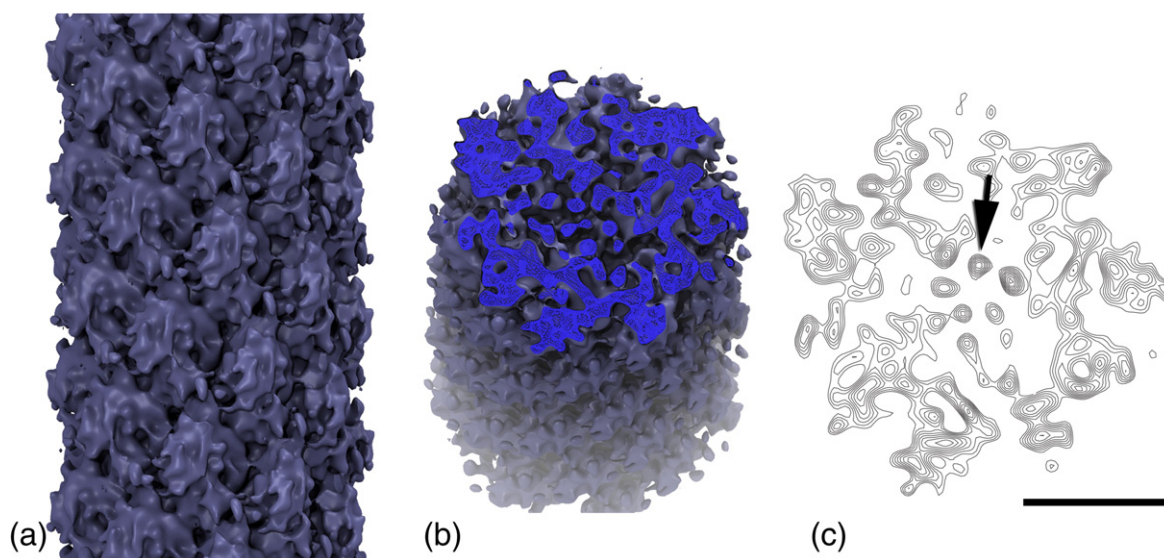


Fig. 4. The surface of a reconstruction of the Iho670 fiber (a and b) and in cross section (c). The cross section (c) shows the nearly vertical rod-like densities (arrow) that are at the center of the volume. The reconstruction has been filtered to 7.5 Å. The space bar in (c) represents 50 Å.

overlapping boxes (each 400 px long, 1.25 Å/px) were used, but the final reconstruction (Fig. 4) was generated from 17,476 segments, with the remainder discarded due to poor alignment statistics. The IHRSR procedure converged to a rotation of 106.65° per subunit and an axial rise of 5.3 Å. The reconstructed volume is ~140 Å in diameter, with large globular domains on the outside and a center containing nearly vertical rod-like densities (Fig. 4c, arrow). These rod-like densities appear to be the N-terminal α -helices, and this arrangement is similar in broad terms to what has been proposed for Type IV pili^{26,42} with two differences: the globular domains are significantly larger in the Iho670 filaments, and the resolution achieved here is unprecedented. The larger globular domains in Iho670 filaments are expected, as the total molecular mass of Iho670 is 33 kDa, while that of a typical bacterial Type IV pilin is ~17 kDa.

To determine the resolution of this reconstruction, we first used the Fourier shell correlation (FSC) approach. While this method is widely used, it has also been noted that it can be quite misleading.^{43,44} The main problem is that the two volumes being compared are rarely independent, since the most common approach (used in Fig. 5) involves aligning both sets of images to a common three-dimensional reference. Thus, noise can become correlated as well as any true signal. Using the more conservative FSC=0.5 criterion,⁴⁵ the resolution suggested (Fig. 5) is a phenomenal 3.75 Å. To obtain a better estimate of resolution, one must use truly separate sets of filament images for the two reconstructions being compared, as opposed to extensively over-

lapped segments.⁴⁶ We have used a molecular modeling approach to derive a more meaningful estimate of the resolution.

Modeling the N-terminus

Secondary structure prediction⁴⁷ shows a strong helix propensity for the N-terminal residues (Fig. 1); hence, we think that it is quite reasonable to assume those residues to be a helix. Given the enantiomorphic

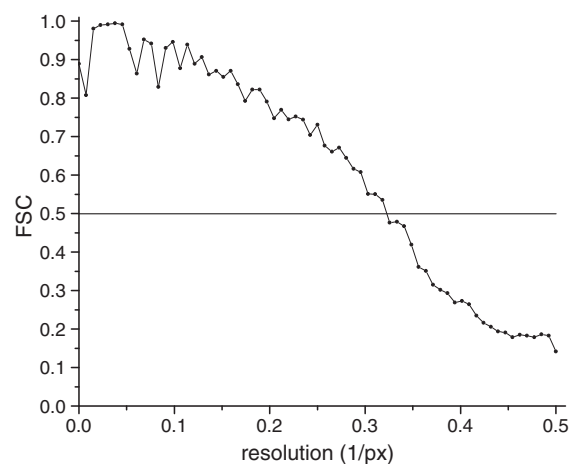


Fig. 5. The FSC is shown between two volumes, each containing half of the 17,476 segments used in the total reconstruction (Fig. 4). Since the sampling is 1.25 Å/px, the “conservative” measure of FSC=0.5 yields a resolution of 1/(3.75 Å), which we can show to be absurd using molecular modeling.

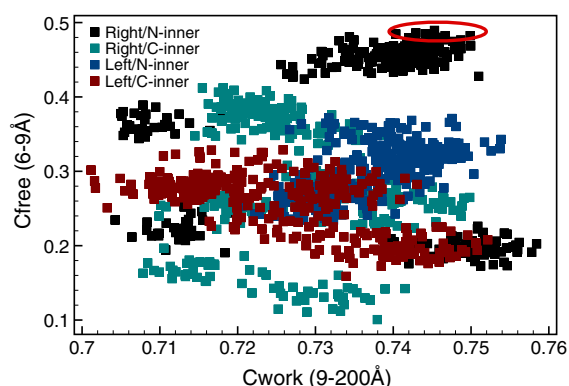


Fig. 6. The correlation coefficient between the model and the density map bandpass filtered between 9 and 200 Å is plotted as C_{work} , while the correlation coefficient between the model and the density map filtered between 6 and 9 Å is plotted as C_{free} . Four different classes of models were used, two having a right-handed one-start helix and two having a left-handed helix, and two having the N-terminus at the inside of the core and two having the N-terminus at the outside of the core.

ambiguity present in the reconstruction, whether the $1/(17.9 \text{ Å})$ layer line is $n=+1$ (right-handed) or $n=-1$ (left-handed), and given the two possible polarities of the helix, four cases were considered: (1) right-handed density, N-terminus at the center of the core; (2) right-handed density, C-terminus of the α -helix at the center of the core; (3) left-handed density, N-terminus at the center of the core; (4) left-handed density, C-terminus of the α -helix at the center of the core. The helix was modeled as a perfect α -helix with all side-chain atoms present.

For the side-chain rotamers, we chose the most probable rotamer in Coot,⁴⁸ which uses the Richardson rotamer library.⁴⁹ This helical model was then kept rigid with tight restraints during the refinement. For each case, 10 different starting positions of the α -helix were generated, which differed only in the rotation around the long axis of the helix; the 10 starting models covered rotation angles between 0° and 360° . This resulted in 40 individual refinements, which were performed using the program DireX.⁵⁰ The α -helix was kept almost rigid using strong restraints during the refinement. A cross-validation approach (details will be published elsewhere) was used to evaluate the fitting, from which we get a C_{work} and a C_{free} value (Fig. 6). The C_{work} value is the cross-correlation of the model density with the experimental density map using the spatial frequency range of 9–200 Å, which was used to perform the fitting. The C_{free} value is obtained with maps bandpass filtered between the frequencies of 6–9 Å, a range that has not been used in the

fitting. Figure 6 shows the $C_{\text{free}}/C_{\text{work}}$ values for the last 30 steps of all 40 fittings.

The best models are those with the highest C_{free} (Fig. 6, red ellipse). These results suggest that the one-start helix is indeed right-handed, as labeled in Fig. 3, and that the N-terminus is located at the very core, with the C-terminal end of this helix leading into the globular domain, as expected. The five best models were virtually identical, and the best is shown (Fig. 7). In addition to the modeling arriving at the correct helix directionality (with the N-terminal end at the core), the axial position of the helix appears to have been found correctly as well, despite the fact that the first two N-terminal amino acids (Val-Ser) are not predicted to form an α -helix and were not used in the fitting described. When these two amino acids are added afterwards, they are contained within the density envelope (Fig. 7), while an incorrect fit of the α -helix to the density map would have shifted the helices down to fill this unoccupied density. This finding provides further support for our model. A comparison between the model and the reconstruction by computing the FSC between a density map derived from the model and the reconstructed density suggests that the actual resolution, at least in the core of the volume, is $\sim 7.5 \text{ Å}$. This shows that the even/odd FSC estimate (Fig. 5) in this instance is hugely overoptimistic and

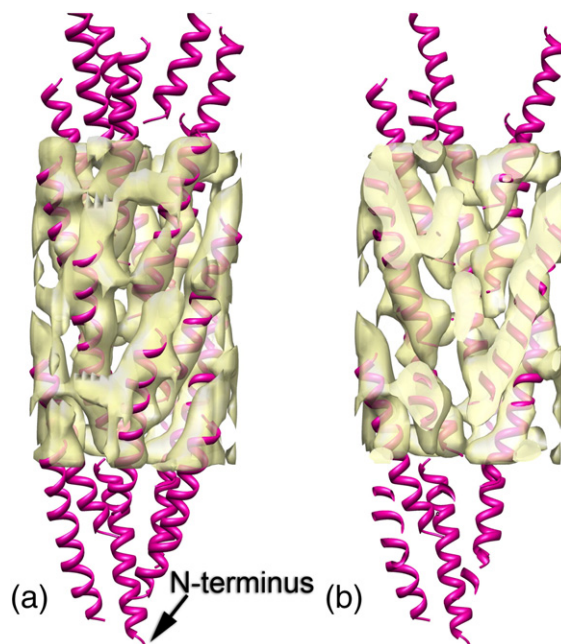


Fig. 7. A model for the packing of the first 26 N-terminal residues in the Iho670 filaments (magenta ribbons) shown with the electron density present within the central core of the filament (transparent yellow surface). The density has been filtered to 7.5 Å . The density and model within a radius of 20 Å from the helical axis are shown in both (a) and (b), but in (b), the front half has been cut away.

suggests that reality checks are frequently needed to properly assess resolution.

Discussion

Our results show unambiguously that the core of the Iho670 filaments contain single α -helices and that the details of the packing of these helices is very different from what has previously been described for the *Neisseria gonorrhoeae* PilE²⁶ and the *Klebsiella oxytoca* PulG⁴² pili. In the case of PilE, the helical parameters were a rotation of 100.8° and an axial rise of 10.5 Å, while for PulG, the parameters were a rotation of 84.7° and an axial rise of 10.4 Å, in contrast to the 106.65° and 5.3 Å that we find for Iho670. These observations support the notion that although all N-terminal hydrophobic helices in these Type IV pilin-like proteins may have a common origin, a large divergence in the quaternary structure of the filaments formed by these proteins has occurred. Similar arguments have been made for bacterial flagellins¹⁵ and bacterial actin-like proteins.^{51–55} In contrast to the case of bacterial flagellins, where the strong conservation of the regions responsible for filament assembly led to the reasonable expectation that the packing of all flagellins would be conserved,³⁵ the substitution of one hydrophobic residue for another in the archaeal homologs of Type IV pilin might lead to less of an expectation for a conserved packing. The loss of a charged residue, Glu5 in bacterial pilins, which is expected to be a key determinant in the packing of Type IV pilins,³⁰ may have also allowed for the large change in quaternary organization of these α -helices. On the other hand, the different symmetry in the Iho670 filament may still mean that a conserved assembly mechanism is shared with the bacterial Type IV pilins.

How similar are the Iho670 filaments to archaeal flagellar filaments? Only two archaeal flagellar filaments have been studied in any structural detail, from *Halobacterium salinarum*^{24,25} and from *Sulfolobus shibatae*.²³ In the case of *H. salinarum*, it was shown that both the twist and axial rise were variable,²⁴ but that the mean symmetry was a 108.0° rotation and a 5.4-Å rise. For *S. shibatae*, the situation was even more complicated, as the filaments could exist either in a purely helical state or as stacks of rings.²³ For the helical state, the symmetry was 108.0° and a rise of 5.3 Å. These symmetries are quite similar to what we observe for the Iho670 filaments (106.65°, 5.3 Å), consistent with our argument that these adhesion fibers are actually similar to the two other archaeal flagellar filaments described so far. The reconstructions of both the *H. salinarum* and the *S. shibatae* filaments were from negatively stained samples, and the resolution was probably limited to 15 Å or worse. At this resolu-

tion, it would be very difficult or impossible to resolve single α -helices; hence, the possibility that coiled coils or protofilaments might exist (both as in the bacterial flagellar filaments) could not be excluded. For the Iho670 filaments, we show that the core can only be composed of single α -helices and that these can only be making interactions with the helices from three or four neighboring subunits. This contrasts with the *Salmonella* flagellar filament, where very strong interactions are made (forming protofilaments) between the coiled coil formed by the N- and C-terminus of subunit *n* and that from *n* + 11. Thus, the mechanism for supercoiling that has been so beautifully established for bacterial flagellar filaments^{10–14} is unlikely to apply to the archaeal flagellar filaments, and these filaments appear to have developed a different mechanism for the supercoiling of helical homopolymers through convergent evolution.

The transitions that we observe between rigid and straight Iho670 filament segments and those with a characteristic curvature (Fig. 2) raise questions about where this switching occurs. The flexural rigidity of a filament will, in general, scale with the fourth power of the radial mass distribution; thus, almost all of the rigidity will be due to the highest radius contacts between protomers in these 140-Å-diameter filaments. An equivalent statement is that the α -helices packed in the core of these filaments (within a radius of 20 Å) will contribute very little to the flexural rigidity. Hence, contacts among the globular outer domains at the highest radii will most likely be involved in the switching that is observed. Understanding how these adhesion filaments can make such transitions, and how archaeal flagellar filaments supercoil, will be the aim of future research.

Materials and Methods

Preparation of the *I. hospitalis* filaments

Growth of cells and preparation of their filaments were as described earlier.³³ In short, this procedure included growth of cells in a 300-L fermenter in the medium described earlier⁵⁶ followed by harvesting the cells via overnight flow-through centrifugation. From the supernatant of this centrifugation, filaments were precipitated overnight at 4 °C (by polyethylene glycol 6000/NaCl addition at 10.5% and 5.8% final concentration, respectively) and harvested by centrifugation (30 min at 10,000g). Aliquots representing 10 L of original fermentation were dissolved in 8 ml buffer; thereafter, 3.6 g of CsCl was added. After CsCl gradient centrifugation (48 h at 250,000g), the resulting band was collected by a 20-gauge needle and filaments were dialyzed against 5 mM 4-morpholineethanesulfonic acid buffer (pH 6.0) containing 1 mM MgSO₄ × 7 H₂O + 1 mM dithiothreitol and stored at 4 °C.

Electron microscopic imaging and analysis

Samples were routinely analyzed by application to glow-discharged, carbon-coated Cu grids, negative staining using uranyl acetate (2% w/v), and imaged in an FEI CM12 TEM at an accelerating voltage of 120 keV, equipped with a TVIPS 0124 CCD camera (1k×1k pixel). For cryo-TEM, fiber samples (3 µl) were applied to freshly glow-discharged C-flat grids, blotted, and plunged into liquid ethane using a home-built cryo-plunger. Grids were imaged using a Tecnai F20 microscope (FEI) at an accelerating voltage of 200 keV and a nominal magnification of 50,000× and recorded on film. Micrographs were scanned with a Nikon Coolsan 8000 at a raster of 1.25 Å per pixel. The helixboxer routine in EMAN⁵⁷ was used for cutting filaments from micrographs. The SPIDER software package⁵⁸ was used for most of the subsequent processing. A negative *B*-factor of 300 Å² was applied to the final volume to compensate for the envelope function of the microscope and other effects that reduce the power in the reconstruction at the highest resolution.

Protein Data Bank accession number

The atomic model has been deposited at the Protein Data Bank with accession code 3J1R. The reconstructed volume has been deposited at the Electron Microscopy Data Bank with accession code 5423.

Acknowledgements

This work was supported by National Institutes of Health grant EB001567 (to E.H.E.) and by WI 731/10-1 from the Deutsche Forschungsgemeinschaft (to R.W. and R.R.).

References

- Asakura, S. (1970). Polymerization of flagellin and polymorphism of flagella. *Adv. Biophys.* **1**, 99–155.
- Trachtenberg, S. & DeRosier, D. J. (1991). A molecular switch: subunit rotations involved in the right-handed to left-handed transitions of *Salmonella typhimurium* flagellar filaments. *J. Mol. Biol.* **220**, 67–77.
- Hyman, H. C. & Trachtenberg, S. (1991). Point mutations that lock *Salmonella typhimurium* flagellar filaments in the straight right-handed and left-handed forms and their relation to filament superhelicity. *J. Mol. Biol.* **220**, 79–88.
- Kamiya, R., Asakura, S. & Yamaguchi, S. (1980). Formation of helical filaments by copolymerization of two types of 'straight' flagellins. *Nature*, **286**, 628–630.
- Kamiya, R. & Asakura, S. (1976). Flagellar transformations at alkaline pH. *J. Mol. Biol.* **108**, 513–518.
- Kamiya, R. & Asakura, S. (1976). Helical transformations of *Salmonella* flagella in vitro. *J. Mol. Biol.* **106**, 167–186.
- Asakura, S., Eguchi, G. & Iino, T. (1966). *Salmonella* flagella: in vitro reconstruction and over-all shapes of flagellar filaments. *J. Mol. Biol.* **16**, 302–316.
- Calladine, C. R. (1978). Change of waveform in bacterial flagella: the role of mechanics at the molecular level. *J. Mol. Biol.* **118**, 457–479.
- Calladine, C. R. (1975). Construction of bacterial flagella. *Nature*, **255**, 121–124.
- Hasegawa, K., Yamashita, I. & Namba, K. (1998). Quasi- and nonequivalence in the structure of bacterial flagellar filament. *Biophys. J.* **74**, 569–575.
- Maki-Yonekura, S., Yonekura, K. & Namba, K. (2010). Conformational change of flagellin for polymorphic supercoiling of the flagellar filament. *Nat. Struct. Mol. Biol.* **17**, 417–422.
- Yonekura, K., Maki-Yonekura, S. & Namba, K. (2003). Complete atomic model of the bacterial flagellar filament by electron cryomicroscopy. *Nature*, **424**, 643–650.
- Samatey, F. A., Imada, K., Nagashima, S., Vonderviszt, F., Kumasaka, T., Yamamoto, M. & Namba, K. (2001). Structure of the bacterial flagellar protofilament and implications for a switch for supercoiling. *Nature*, **410**, 331–337.
- Yamashita, I., Hasegawa, K., Suzuki, H., Vonderviszt, F., Mimori-Kiyosue, Y. & Namba, K. (1998). Structure and switching of bacterial flagellar filaments studied by X-ray fiber diffraction. *Nat. Struct. Biol.* **5**, 125–132.
- Galkin, V. E., Yu, X., Bielnicki, J., Heuser, J., Ewing, C. P., Guerry, P. & Egelman, E. H. (2008). Divergence of quaternary structures among bacterial flagellar filaments. *Science*, **320**, 382–385.
- Mimori-Kiyosue, Y., Vonderviszt, F., Yamashita, I., Fujiyoshi, Y. & Namba, K. (1996). Direct interaction of flagellin termini essential for polymorphic ability of flagellar filament. *Proc. Natl Acad. Sci. USA*, **93**, 15108–15113.
- Vonderviszt, F., Aizawa, S. & Namba, K. (1991). Role of the disordered terminal regions of flagellin in filament formation and stability. *J. Mol. Biol.* **221**, 1461–1474.
- Thomas, N. A. & Jarrell, K. F. (2001). Characterization of flagellum gene families of methanogenic archaea and localization of novel flagellum accessory proteins. *J. Bacteriol.* **183**, 7154–7164.
- Thomas, N. A., Bardy, S. L. & Jarrell, K. F. (2001). The archaeal flagellum: a different kind of prokaryotic motility structure. *FEMS Microbiol. Rev.* **25**, 147–174.
- Thomas, N. A., Pawson, C. T. & Jarrell, K. F. (2001). Insertional inactivation of the *flaH* gene in the archaeon *Methanococcus voltae* results in non-flagellated cells. *Mol. Genet. Genomics*, **265**, 596–603.
- Bayley, D. P. & Jarrell, K. F. (1998). Further evidence to suggest that archaeal flagella are related to bacterial type IV pili. *J. Mol. Evol.* **46**, 370–373.
- Szabo, Z., Stahl, A. O., Albers, S. V., Kissinger, J. C., Driessen, A. J. & Pohlschroder, M. (2007). Identification of diverse archaeal proteins with class III signal peptides cleaved by distinct archaeal prepilin peptidases. *J. Bacteriol.* **189**, 772–778.
- Cohen-Krausz, S. & Trachtenberg, S. (2008). The flagellar filament structure of the extreme acidothermophile *Sulfolobus shibatae* B12 suggests that archaeobacterial flagella have a unique and common symmetry and design. *J. Mol. Biol.* **375**, 1113–1124.
- Trachtenberg, S., Galkin, V. E. & Egelman, E. H. (2005). Refining the structure of the *Halobacterium salinarum* flagellar filament using the iterative helical

- real space reconstruction method: insights into polymorphism. *J. Mol. Biol.* **346**, 665–676.
25. Cohen-Krausz, S. & Trachtenberg, S. (2002). The structure of the archaeobacterial flagellar filament of the extreme halophile *Halobacterium salinarum* R1M1 and its relation to eubacterial flagellar filaments and type IV pili. *J. Mol. Biol.* **321**, 383–395.
 26. Craig, L., Volkmann, N., Arvai, A. S., Pique, M. E., Yeager, M., Egelman, E. H. & Tainer, J. A. (2006). Type IV pilus structure by cryo-electron microscopy and crystallography: implications for pilus assembly and functions. *Mol. Cell*, **23**, 651–662.
 27. Forest, K. T. & Tainer, J. A. (1997). Type-4 pilus-structure: outside to inside and top to bottom—a minireview. *Gene*, **192**, 165–169.
 28. Parge, H. E., Forest, K. T., Hickey, M. J., Christensen, D. A., Getzoff, E. D. & Tainer, J. A. (1995). Structure of the fibre-forming protein pilin at 2.6 Å resolution. *Nature*, **378**, 32–38.
 29. Pelicic, V. (2008). Type IV pili: e pluribus unum? *Mol. Microbiol.* **68**, 827–837.
 30. Craig, L., Pique, M. E. & Tainer, J. A. (2004). Type IV pilus structure and bacterial pathogenicity. *Nat. Rev. Microbiol.* **2**, 363–378.
 31. Albers, S. V., Szabo, Z. & Driessen, A. J. (2003). Archaeal homolog of bacterial type IV prepilin signal peptidases with broad substrate specificity. *J. Bacteriol.* **185**, 3918–3925.
 32. Pohlschroder, M., Ghosh, A., Tripepi, M. & Albers, S. V. (2011). Archaeal type IV pilus-like structures—evolutionarily conserved prokaryotic surface organelles. *Curr. Opin. Microbiol.* **14**, 357–363.
 33. Müller, D. W., Meyer, C., Gürster, S., Küper, U., Huber, H., Rachel, R. *et al.* (2009). The Iho670 fibers of *Ignicoccus hospitalis*: a new type of archaeal cell surface appendage. *J. Bacteriol.* **191**, 6465–6468.
 34. Thompson, J. D., Higgins, D. G. & Gibson, T. J. (1994). CLUSTAL W: improving the sensitivity of progressive multiple sequence alignment through sequence weighting, position-specific gap penalties and weight matrix choice. *Nucleic Acids Res.* **22**, 4673–4680.
 35. Beatson, S. A., Minamino, T. & Pallen, M. J. (2006). Variation in bacterial flagellins: from sequence to structure. *Trends Microbiol.* **14**, 151–155.
 36. Hansen, J. K. & Forest, K. T. (2006). Type IV pilin structures: insights on shared architecture, fiber assembly, receptor binding and type II secretion. *J. Mol. Microbiol. Biotechnol.* **11**, 192–207.
 37. Meyer, C. (2010). Die Fibrillen von *Ignicoccus hospitalis*: Ultrastruktur, Verankerung und molekularbiologische Untersuchungen. University of Regensburg, Regensburg, Germany.
 38. Rivetti, C., Guthold, M. & Bustamante, C. (1996). Scanning force microscopy of DNA deposited onto mica: equilibrium versus kinetic trapping studied by statistical polymer chain analysis. *J. Mol. Biol.* **264**, 919–932.
 39. Yu, X. & Egelman, E. H. (2010). Helical filaments of human Dmc1 protein on single-stranded DNA: a cautionary tale. *J. Mol. Biol.* **401**, 544–551.
 40. Egelman, E. H. (2010). Reconstruction of helical filaments and tubes. *Methods Enzymol.* **482**, 167–183.
 41. Egelman, E. H. (2000). A robust algorithm for the reconstruction of helical filaments using single-particle methods. *Ultramicroscopy*, **85**, 225–234.
 42. Campos, M., Nilges, M., Cisneros, D. A. & Francetic, O. (2010). Detailed structural and assembly model of the type II secretion pilus from sparse data. *Proc. Natl Acad. Sci. USA*, **107**, 13081–13086.
 43. Yang, S., Yu, X., Galkin, V. E. & Egelman, E. H. (2003). Issues of resolution and polymorphism in single-particle reconstruction. *J. Struct. Biol.* **144**, 162–171.
 44. Grigorieff, N. (2000). Resolution measurement in structures derived from single particles. *Acta Crystallogr. D Biol. Crystallogr.* **56**(Pt 10), 1270–1277.
 45. Rosenthal, P. B. & Henderson, R. (2003). Optimal determination of particle orientation, absolute hand, and contrast loss in single-particle electron cryomicroscopy. *J. Mol. Biol.* **333**, 721–745.
 46. Galkin, V. E., Orlova, A., Salmazo, A., Djinoivic-Carugo, K. & Egelman, E. H. (2010). Opening of tandem calponin homology domains regulates their affinity for F-actin. *Nat. Struct. Mol. Biol.* **17**, 614–616.
 47. Jones, D. T. (1999). Protein secondary structure prediction based on position-specific scoring matrices. *J. Mol. Biol.* **292**, 195–202.
 48. Emsley, P. & Cowtan, K. (2004). Coot: model-building tools for molecular graphics. *Acta Crystallogr. D Biol. Crystallogr.* **60**, 2126–2132.
 49. Lovell, S. C., Word, J. M., Richardson, J. S. & Richardson, D. C. (2000). The penultimate rotamer library. *Proteins*, **40**, 389–408.
 50. Schröder, G. F., Brunger, A. T. & Levitt, M. (2007). Combining efficient conformational sampling with a deformable elastic network model facilitates structure refinement at low resolution. *Structure*, **15**, 1630–1641.
 51. Galkin, V. E., Orlova, A., Rivera, C., Mullins, R. D. & Egelman, E. H. (2009). Structural polymorphism of the ParM filament and dynamic instability. *Structure*, **17**, 1253–1264.
 52. Polka, J. K., Kollman, J. M., Agard, D. A. & Mullins, R. D. (2009). The structure and assembly dynamics of plasmid actin AlfA imply a novel mechanism of DNA segregation. *J. Bacteriol.* **191**, 6219–6230.
 53. Orlova, A., Garner, E. C., Galkin, V. E., Heuser, J., Mullins, R. D. & Egelman, E. H. (2007). The structure of bacterial ParM filaments. *Nat. Struct. Mol. Biol.* **14**, 921–926.
 54. Popp, D., Narita, A., Ghoshdastider, U., Maeda, K., Maeda, Y., Oda, T. *et al.* (2010). Polymeric structures and dynamic properties of the bacterial actin AlfA. *J. Mol. Biol.* **397**, 1031–1041.
 55. Popp, D., Xu, W., Narita, A., Brzoska, A. J., Skurray, R. A., Firth, N. *et al.* (2010). Structure and filament dynamics of the pSK41 actin-like ParM protein: implications for plasmid DNA segregation. *J. Biol. Chem.* **285**, 10130–10140.
 56. Paper, W., Jahn, U., Hohn, M. J., Kronner, M., Näther, D. J., Burghardt, T. *et al.* (2007). *Ignicoccus hospitalis* sp. nov., the host of 'Nanoarchaeum equitans'. *Int. J. Syst. Evol. Microbiol.* **57**, 803–808.
 57. Ludtke, S. J., Baldwin, P. R. & Chiu, W. (1999). EMAN: semiautomated software for high-resolution single-particle reconstructions. *J. Struct. Biol.* **128**, 82–97.
 58. Frank, J., Radermacher, M., Penczek, P., Zhu, J., Li, Y., Ladjadj, M. & Leith, A. (1996). SPIDER and WEB: Processing and visualization of images in 3D electron microscopy and related fields. *J. Struct. Biol.* **116**, 190–199.